Editors' Suggestion

Confinement of magnetic solitons and edge states in a van der Waals material: FeOCl

Martin Panthöfer,[1] Stefanie Berinskat,[1] Fabian Predelli,[2] Peter Lemmens,[2,3] and Angela Möller[1,*]
[1]*Department of Chemistry, Johannes Gutenberg-University Mainz, Duesbergweg 10-14, 55128 Mainz, Germany*
[2]*Institute of Condensed Matter Physics, TU Braunschweig, Mendelssohnstr. 3, 38106 Braunschweig, Germany*
[3]*Laboratory for Emergent Nanometrology (Lena), TU Braunschweig, Langer Kamp 6, 38106 Braunschweig, Germany*

(Received 31 January 2024; revised 10 March 2024; accepted 20 March 2024; published 15 April 2024)

In a comparative and systematic study on finite-size particles the isostructural van der Waals materials ScOCl, ScOBr, and FeOCl, are investigated. The origin of unconventional magnetic properties of FeOCl ($S = 5/2$) is elucidated. Experimental evidence for fluctuations are presented and discussed in relation to soliton condensation into topological edge states. The anisotropy within $^{2}_{\infty}[FeO_{4/4}Cl_{2/2}]$ corrugated layers gives rise to the formation of solitons (1D) with parameters given here and to the development of 2D-Ising magnetic order around 20 K. The latter is identified by a λ anomaly in the specific heat and a kink in the magnetic susceptibility. Concomitantly, the canting angle of moments along the spin-chain direction changes. We attribute this to a magnetoelastic effect. The finite size of the chains (≈143 Fe-sites ≈ ξ_s at 20 K) results in the confinement of solitons, which condense into breathers. In small applied magnetic fields the dynamics unfold and a spin-glass-like phase below 5 K is established. Phonon anharmonicities revealed by Raman scattering are explained by diffusional dynamics and are in agreement with the derived soliton energy from Mössbauer spectroscopy.

DOI: 10.1103/PhysRevMaterials.8.044003

I. INTRODUCTION

The interest in van der Waals (vdW) materials intensified in the last decade with a focus on their fascinating mechanical, optical, and electronic properties. These arise from the inherent high anisotropy of layered materials in conjunction with tuneable layer thickness with relevance to applications. More recently, unprecedented mechanical strength and acoustically driven magnon-phonon coupling was demonstrated for $CrCl_3$ [1]. In particular, the magnetic vdW materials of the *M*OCl-type with M = Cr or Fe have been identified as candidates for studies on size effects in connection with spin degrees of freedom, e.g., magnetoelastic effects, spintronics, and multiferroicity [2–7]. Potential catalytic properties are also reported [8].

More fundamental questions address the controlled dimensionality, which can lead to confinement effects and interplay with inherent fluctuations of low-dimensional systems [9–11]. Size-dependent topological excitations have been observed, e.g., in transport data due to gapped $S = 1/2$ edge states of $S = 1$ chains [12]. Important aspects of edge states are nonlinear phenomena due to spin-orbit coupling [13], anisotropies, and a dissipative bath, e.g., due to phonons [1].

In principle, at the boundaries of magnetic low-dimensional systems domain-wall-like or kink modes exist. Given the inherent anisotropy in multi-anionic vdW materials (e.g., FeOCl), soliton and spinon excitations may govern the magnetic response of a material within the underlying spin chains and their interchain exchange. Solitons in magnetic chains represent kink-like nonlinear excitations [14–16] with experimental studies on the spin dynamics given in [17–20]. More recently, finite-size characteristics were reported with respect to confinement, e.g., breather modes [21–23]. The dynamics of such states are in the center of our present paper on FeOCl.

Early studies provide insights into the thermodynamic stability and formation of red needle-shaped crystals of FeOCl [24]. The physical properties have been studied on large crystals using Mössbauer spectroscopy [25–30], Raman scattering [2,4], magnetic susceptibility (mostly in rather high magnetic fields of 1 T) [31,32], specific heat measurements in zero applied magnetic fields [32], by neutron diffraction [33,34], and synchrotron experiments [32].

^{57}Fe Mössbauer spectroscopic investigations show that significant dynamics of the $S = 5/2$ spin system persists even below the claimed long range ordering temperature T_N in the range 81–92 K as suggested from methods listed above. However, study on microcrystalline powder samples reveal only a kink in the magnetic susceptibility at ≈20K [31]. Specific heat measurements performed on large crystals support a higher ordering temperature [32]. However, the related λ anomaly amounts to only 1% of the expected magnetic entropy. Quasi-elastic magnetic Raman scattering due to the evolution of correlations has been reported with a polarization perpendicular to the direction of dominant exchange [2]. This is an unconventional observation. Neutron diffraction experiments reveal a spin-spiral magnetic structure with an incommensurate order parameter that leads to a 99° canting between adjacent spin chains within the Fe–O layers of this vdW material at 4.2 K [33]. It has been observed that the structural modulation vector is temperature dependent above 30 K [32]. These observations indicate that the evolution of magnetism in FeOCl is presently not well understood and that the compound deserves further investigation.

*angela.moeller@uni-mainz.de

In the present experimental study we have performed a systematic investigation of the vdW family of microcrystalline compounds, ScOCl, ScOBr, and FeOCl, with the focus on size-related and inherently unconventional magnetic instabilities relating to spin dynamics for FeOCl. ScOCl and ScOBr are investigated as nonmagnetic reference systems.

II. EXPERIMENTAL

FeOCl was obtained from reacting 3–5 mmol Fe_2O_3 (99,9%, ChemPur) with a 12-fold molar excess of conc. HCl (37 wt%, VWR Chemicals). The solution was heated at 240 °C for 1 h and the resulting solid dried in vacuum (10^{-2} mbar) for 1 d at room temperature. As a side remark, above 300 °C Fe_2O_3 impurities form. $ScOX (X = Cl, Br)$ were obtained by dissolution of Sc metal (99.9%, Smart Elements) in conc. HCl (37 wt%) and HBr (48 wt%, AlfaAesar), respectively. Typically, 5 to 10 mmol Sc were used with a 10-fold molar excess of the acid. The solution was heated to 300 °C in open ampules (approx. 10–15 cm length) for at least 3.5 h in order to avoid formation of the tetrahydrate. All products were handled under inert gas atmospheres (Schlenk line or glove box, MBraun) after heat treatment and cooling to 120 °C and for sample preparation for physical property measurements. Scanning electron microscope (SEM) photographs were taken in charge reduction mode using a Phenom ProX benchtop electron microscope (Thermo Fisher Scientific GmbH).

Powder diffraction data were collected with a STOE Stadi E goniometer operating in Debye-Scherrer mode (fine focus Mo x-ray tube, Ge(111) monochromator, $\lambda = 0.7093$ Å, Dectris Mythen 1k detector). All samples were handled in sealed Lindemann-glass capillaries to avoid degradation by humidity.

Magnetization and specific heat measurements were conducted at temperatures from 2–300 K in applied magnetic fields up to 8 T using a PPMS system (DynaCool-9, Quantum Design).

^{57}Fe Mössbauer spectra were recorded with a custom built system in transmission mode. The spectrometer was calibrated to α-Fe foil at room temperature. A well-ground sample of FeOCl was dispersed into paraffin, spread in a PE container of 1.6 cm inner diameter and placed in a brass holder, thermally contacted to a close cycle cryostat (C2, Montana Instruments). Spectral analysis was performed using the software package Recoil [35] applying the extended Voigt based fitting approach xVBF [36], the full static hamiltonian approach for magnetic spectra, and the Tjon-Blume model [37] to extract flip frequencies in the fast relaxation regime.

Electric fields gradients (EFG) [38] were computed with CASTEP 21.11 [39] using the PBE for Solids GGA [40], on-the-fly ultrasoft pseudopotentials and a cutoff energy of $E_{\text{cutoff}} = 1001.38$ eV. Crystal structure data from this paper were used without further relaxation. EFGs and resulting quadrupole splitting were carefully tested for convergence upon number of k points (spacing, 0.01 Å^{-1}; grid, $31 \times 27 \times 13$; k points, 1568).

Raman scattering experiments have been performed on powder samples of ScOBr, ScOCl, and FeOCl as a function of temperature in the range 5–300 K. We used a microscope cryostat (CryoVac), a LabRAM HR800 micro Raman setup (Horiba Jobin Yvon), and a Nd-YAG solid state laser (excitation at 532 nm). The supernotch filter leads to an excellent suppression of stray light down to Raman shifts of 10 cm^{-1}. The large aperture of the sampling optics (50x, Olympus) and the nonoriented powder agglomerates of the samples allowed detecting all symmetry allowed phonon modes in a single scattering experiment.

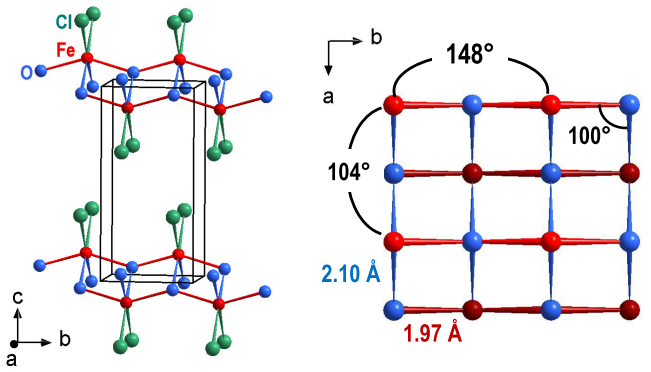

FIG. 1. (Left) Crystal structure of FeOCl. (Right) Projection of a corrugated Fe/O layer along the c axis. Chains are highlighted in red stick representation while interchain connectivity is given in blue. Selected angles and interatomic distances are labeled.

III. RESULTS AND DISCUSSION

A. X-ray diffraction

In Fig. 1 we show the crystal structure of FeOCl. The samples were evaluated with respect to their morphology in order to gain insights into finite-size effects. In Fig. 2 Rietveld refinements of x-ray powder diffraction data are depicted for ScOCl and FeOCl along with typical scanning electron microscopic (SEM) photographs. ScOCl and ScOBr (not shown here) gave similar results. Full profile pattern fits were performed in the framework of the funda-

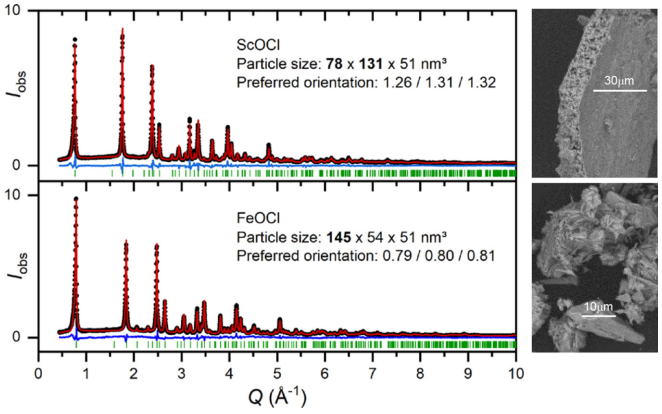

FIG. 2. (Left) Rietveld refinement of x-ray powder diffraction data for ScOCl ($R_{\text{wp}} = 7.24$) and FeOCl ($R_{\text{wp}} = 7.33$). Experimental data (black dots), fit (red line), difference line (blue line) and Bragg positions (green bars). Particle sizes and preferred orientation are included in the insets. SEM photographs of ScOCl (top, right) and FeOCl (bottom, right).

TABLE I. Crystallographic data for ScOCl, ScOBr, and FeOCl. Space group *Pmmn* (standard setting, cell choice 2), $Z = 2$, Wyckoff positions: M(2*b*), O(2*a*), and X(2*a*).

	ScOCl	ScOBr	FeOCl
a (Å)	3.4492(1)	3.4793(8)	3.2933(1)
b (Å)	3.96001(9)	3.9590(9)	3.7745(1)
c (Å)	8.1324(3)	8.730(2)	7.8997(3)
M $(\frac{1}{4}, \frac{3}{4}, z)$	0.1161(2)	0.105(1)	0.1168(2)
O $(\frac{1}{4}, \frac{1}{4}, z)$	0.0375(5)	0.051(3)	0.0472(6)
X $(\frac{1}{4}, \frac{1}{4}, z)$	0.6675(2)	0.6671(7)	0.6736(3)

mental parameter approach (background: Chebyshev, profile: fundamental parameters) as implemented in TOPAS Academic V7 software [41]. Anisotropic reflection broadening due to the morphology was handled by computing individual crystallite sizes [$CS(h)$] for each reflection h according to the quadratic form $CS(h) = 1/\text{norm} \cdot h^T \cdot C_{ij} \cdot h$, with $C_{ij} = \sqrt{a_i} \times \sqrt{a_j}$ as the symmetric second rank tensor of the square roots of the crystallite dimensions, a, in the directions i and j corresponding to the basis of the crystal lattice ($a_1 = \vec{a}, a_2 = \vec{b}$, and $a_3 = \vec{c}$). All three vdW compounds exhibit almost equal sizes in [001], which translates into ≈60 layers. Crystallographic data is listed in Table I. The lattice parameters are in agreement with the literature [42–44]. In Fig. 1 we show the crystal structure.

It is interesting to note, that the Sc samples exhibit a morphology of platelets growing perpendicular to the c axis as expected for layered compounds with layers in the ab plane. Here, the growth rate along the b direction exceeds the one along the shorter a axis, which may be tentatively related to the difference in the Sc–Sc connectivity to O-bridged chains in the former and (O,Cl) edges in the latter case, see also Fig. 1. Contrarily, FeOCl crystallites grow as needles as a result of the antiferromagnetic –O–Fe–O–Fe– chains in the [010] direction. This formally doubles the b axis and thus results in $b' = 2b_0 \approx c$. At the same time the growth in the a direction is pronounced as a is the shortest axis.

B. Specific heat

The specific heat capacity for ScOCl, ScOBr, and FeOCl is shown in Fig. 3(a). With respect to the phonon contribution it is obvious that the difference between ScOCl and ScOBr stems from the heavier bromide and results in a weight shift to lower characteristic temperatures for the bromide. We have applied a model proposed by Ref. [45] and fitted our data to one Debye (acoustic branch) and two Einstein modes, which refer to the optical branches of M-O(M = Sc, Fe) and M-Cl or Sc-Br, respectively. Table II lists the derived temperatures ($\Theta_D, \Theta_{E1}, \Theta_{E2}$). The successful modeling of ScOCl and ScOBr allows us to distinguish lattice from magnetic contributions to C_p(T) for FeOCl.

The magnetic part of the specific heat in zero-field for FeOCl is obtained by subtracting the phonon contribution, Fig. 3(b). C_m(T) follows the typical form of a low-dimensional spin system with spin correlations extending to high temperatures and exhibits a broad maximum around 75 K. The

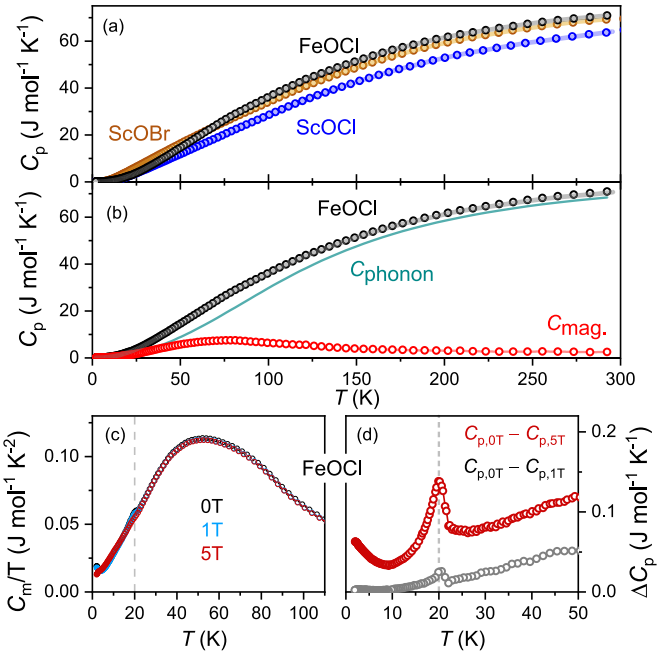

FIG. 3. (a) Temperature dependence of the specific heat (circles) for ScOCl, ScOBr, and FeOCl, individual fits are presented by lines. (b) Phonon and magnetic contribution to the specific heat for FeOCl in zero applied magnetic field. (c) Temperature dependence of C_m/T in zero and applied magnetic fields. (d) Difference of the specific heat for FeOCl in applied magnetic fields. The red data points are shifted by 0.05 Jmol^{-1}K^{-1}.

derived magnetic entropy, $S_m(\text{T}) = \int_2^{292} C_m/T\,dT$, yields 82% of the expected total value of $R \cdot \ln(2S + 1)$ with $S = 5/2$ for high-spin Fe^{III}.

It is interesting to note that for large crystals of FeOCl a small λ anomaly (1% of the total S_m) around 82 K has been observed [32]. In the case of finite-size particles under investigation here, this feature is absent, see Figs. 3(b) and 3(c). Instead we find evidence for a small anomaly at 20 K in zero field [Fig. 3(c)]. By subtracting the measured C_p(T) data collected in different applied magnetic fields from the zero-field data [Fig. 3(d)], we gain the following insights. The λ anomaly is slightly reduced in applied magnetic fields of 1 T, $\Delta C_{p,(0T-1T)}$. Since this feature is absent in the $C_{p,5T}$ data, $\Delta C_{p,(0T-5T)}$ documents the presence of the λ anomaly at 20 K in zero field. Furthermore, it can be seen that the magnetic entropy associated with the λ anomaly is shifted to lower temperatures in the case of $C_{p,5T}$, compare also to

TABLE II. Analysis of phonon contribution to the specific heat capacity for ScOBr, ScOCl, and FeOCl using a fit model consisting of one Debye and two Einstein modes given in units of Kelvin and numbers are given in brackets.

	ScOCl	ScOBr	FeOCl
Θ_D (n_D)	160 (1.8)	110 (1.6)	160 (1.1)
Θ_{E1} (n_{E1})	306 (3.0)	230 (2.9)	260 (2.4)
Θ_{E2} (n_{E2})	624 (4.4)	560 (5.3)	470 (6.0)

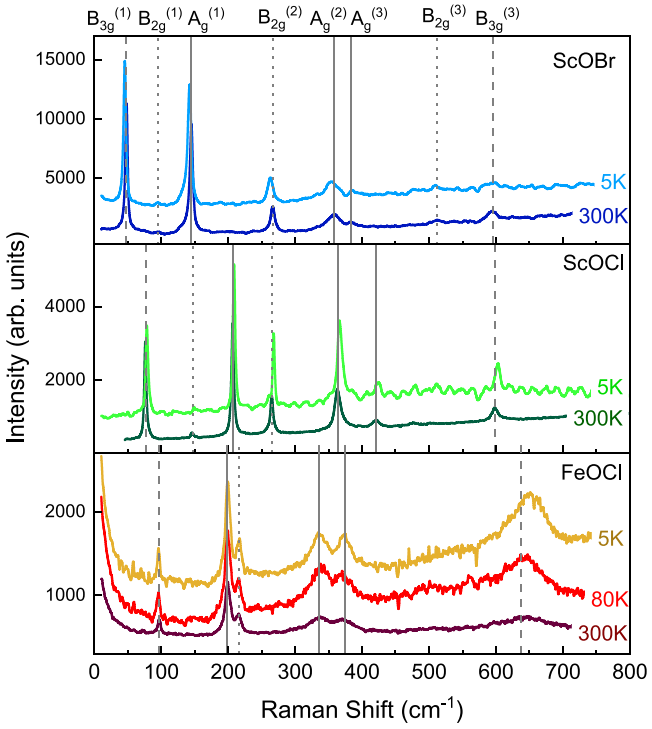

FIG. 4. Raman spectra at selected temperatures for ScOBr, ScOCl, and FeOCl. The spectra are vertically shifted for different temperatures. Modes are labeled according to Table III and marked by gray lines representing A_g (solid), B_{2g} (dotted), and B_{3g} (dashed) for comparison.

Fig. 3(c). We will discuss the field dependence in more detail in the context of the magnetic properties further below.

C. Raman spectroscopy

Temperature resolved Raman spectra are presented in Fig. 4 and properties of the resolved phonon modes are given in Table III. The group theoretical analysis of MOX based on the crystallographic data leads to one A_g, one B_{2g}, one B_{3g} for each ion, and a sum of $3 \cdot A_g + 3 \cdot B_{2g} + 3 \cdot B_{3g} = 9$ Raman active modes, according to Ref. [46]. In our experiments on powder samples all modes of sufficient scattering intensity may be observed and can be compared in a single experiment.

TABLE III. Mode frequencies and linewidths (FWHM) at T = 300 K with their assignment to symmetry allowed phonons, "–" corresponds to the nonobservation of a mode.

	Mode frequency and linewidth (cm^{-1})					
Mode	ScOCl		ScOBr		FeOCl	
$A_g(1)$	208	4.0	145	5.4	199	9.0
$A_g(2)$	364	11.1	358	26.3	336	28.2
$A_g(3)$	421	9.3	383	10.6	374	32.4
$B_{2g}(1)$	147	4.2	95	6.2	–	–
$B_{2g}(2)$	266	5.1	267	7.4	216	9.4
$B_{2g}(3)$	–		512	12.4	–	–
$B_{3g}(1)$	77	3.5	48	3.5	97	4.9
$B_{3g}(2)$	–	–	–	–	–	–
$B_{3g}(3)$	599	11.1	595	13.6	638	71

The mode frequencies and linewidths (FWHM) presented in Table III result from a fit to Raman spectra using Lorentzian and Gaussian functions. These mode data are given in groups according to the symmetry representation and the additional numbering. According to previous dynamical lattice calculations the A_g, B_{2g}, and B_{3g} modes correspond to displacements along the c, a, and b axis, and the numbering (1) to (3) refer to dominant halide, metal, and oxide displacements [47]. This specific relation allows to draw conclusions about microscopic electron-phonon coupling of the modes. An entry "–" corresponds to an assumed nonobservation of a mode. This is either due to their weak intensity and/or due to an overlap with a different mode of similar frequency. The latter case holds for $B_{2g}(2)$ and $B_{3g}(2)$ modes. Our data and phonon assignment are in good agreement with previous single crystals studies and dynamical lattice calculations of TiOCl and VOCl [46–49].

Based only on the above given symmetry analysis we only expect gradual differences between the compounds. However, for FeOCl anomalous properties of the higher frequency excitations are evident, see Fig. 4.

The exchange of halides may have an effect on phonon modes that involve mainly such Cl and Br displacements. The $A_g(1)$ and the $B_{3g}(1)$ show frequency decreases of 30% and 37%, respectively, while $A_g(3)$ shows only an effect of 9%. Here, the mode linewidth is not altered. The exchange of the transition metal ions leads to a moderate frequency decrease with the atomic mass of the ion of the A_g modes. The smallest frequencies are observed for M = Fe and the $A_g(2)$. The shift from ScOCl to FeOCl corresponds to the expected 11%.

In Fig. 4 the Raman spectra of the studied MOX compounds are shown at two temperatures (5 and 300 K). It is noticeable that the low frequency modes of all compounds have a Lorentzian lineshapes and small linewidths of 4–5 cm^{-1}. This points to a high sample quality. In the case of FeOCl all modes with frequencies approximately above 300 cm^{-1} are broadened. These modes are related to oxygen displacements that themselves couple to the superexchange of Fe. The phonon linewidth is usually inversely related to the phonon lifetime. The latter is limited by decay processes of optical phonons into two or three acoustic phonons with opposite and large momenta [50]. The maximum energy of these decay partners depends only on the averaged ionic masses of the MOX compounds. Therefore, this mechanism leads to a moderate dependence of linewidth on the transition metals. This process is only effective for large energy modes.

A direct comparison of the spectra in Fig. 4, shows that there exist further effects. The high energy modes of FeOCl at 336, 374, and 638 cm^{-1}, attributed to $A_g(2)$, $A_g(3)$, and $B_{3g}(3)$, show a Gaussian-like lineshape with large linewidth and intensity. Such a Gaussian lineshape is rather uncommon. Previous spectroscopic studies of different nanomaterials have only found broadened, asymmetrical Lorentzians as a result of phonon confinement or structural disorder [51,52]. Therefore, such an explanation has to be ruled out. In TiOCl a comparably large intensity of B_{3g} modes has been attributed to higher order Raman scattering processes [47]. Such excitations gain

TABLE IV. Analysis of the ^{57}Fe Mössbauer spectrum at 3.3 K for FeOCl ($\chi^2 = 1.57$). Fixed hyperfine parameters: center shift $\delta = 0.511$ mm/s, linewidth HWHM $\Gamma_{1/2} = 0.160$ mm/s, $\theta_{\rm Hq} = 90°$. Refined hyperfine parameters: quadrupole coupling constant (ϵ), hyperfine field $H_{\rm hf}$, $\phi_{\rm Hq}$, and site fractions.

Site	$H_{\rm hf}$ (kOe)	ϵ (mm/s)	η	$\phi_{\rm Hq}$ (deg)	frac. (%)
1	437.9(1)	0.164	0.01	90	35.9
2	425.5(1)	0.189	0.17	88(3)	26.4
3	409.5(3)	0.212	0.36	46(1)	16.1
4	388.8(8)	0.167	0.36	30(4)	6.9
5	449.8(4)	0.124	0.36	0	12.9
6	70(5)	0.210	0.36	0	1.8

the symmetry $A_g =: (B_{3g} \otimes B_{3g})$ leading to larger intensities in the given scattering geometry.

The above mentioned modes of FeOCl at 336, 374, and 638 cm^{-1} have linewidths of 28, 32, and 71 cm^{-1}, respectively. The latter is a factor 8 larger than the linewidths of low-frequency modes of FeOCl and a factor of 6 larger than the respective highest frequency mode of ScOCl. Therefore, we state that phonons in FeOCl suffer from an additional decay process. The observed Gaussian lineshape points to nonequilibrium states that relax with a diffusional dynamics [53]. Gaussian functions are the solution of Fokker-Planck or Langevin equations that describe stochastic processes of systems that evolve due to a combination of deterministic and fluctuating forces [54]. Such fluctuations are also well known from relaxation processes in low-dimensional systems where conventional fluctuations of energy density and phase transitions are suppressed [55].

Assuming independent scattering processes, the resulting phonon linewidth is then given by the sum of inverses of lifetimes that represent conventional phonon anharmonicity and a process based on diffusional dynamics $\tau_{\rm sum}^{-1} = \tau_{\rm phonon}^{-1} + \tau_{\rm diff}^{-1}$ [56]. Subtracting our experimental data of B_{3g} linewidths in ScOCl and FeOCl, we obtain $\Gamma_{\rm diff} = 60$ cm$^{-1} \approx 80$ K. This linewidth compares well to the fluctuating energy scale leading to the nonequilibrium state, see below. Further evidence for low-dimensional fluctuations in FeOCl are given by the quasi-elastic scattering in Fig. 4, i.e., the intensity observed at very small energies with a Lorentzian frequency dependence, see also [2]. The respective scattering intensity shows an uprise to lower temperature and no drop below ≈80 K. This is in accordance with a continuous evolution of magnetic correlations at low temperature and contrasts conventional LRO at low temperatures.

D. ^{57}Fe Mössbauer spectroscopy

We investigated FeOCl with a local probe (^{57}Fe Mössbauer spectroscopy) especially appropriate to unravel local fluctuations. In Fig. 5 the measured Mössbauer spectra are shown in the temperature range 3.3–300 K. Temperature-dependent hyperfine parameters are given in Fig. 6. For method specific details, we refer to Ref. [57,58] and the Appendix listing equations [Eqs. (A1)–(A3)] used in the data analysis.

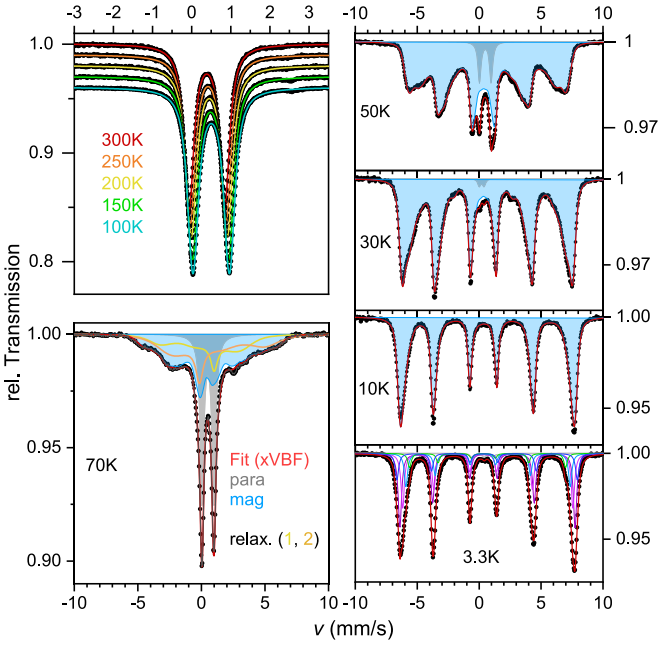

FIG. 5. ^{57}Fe Mössbauer transmission spectra for FeOCl: experimental data (black dots) and individual fitted spectra (colored lines, $100 \leqslant T \leqslant 300$ K). Below 100 K the blue shaded areas mark the magnetic and the small grey shaded areas the vanishing paramagnetic (fast relaxing) spectral contribution. The spectrum at 70 K contains the reference (orange, yellow lines) to the two magnetic subspectra with different relaxation rates. At 3.3 K the static magnetic order is composed of individual subspectra, see Table IV.

In the paramagnetic regime between 100 and 300 K, we observe a doublet, which is characterized by the center (or chemical) shift δ and the quadrupole splitting QS, Figs. 6(a) and 6(b). The center shift corresponds to the electric monopole interaction and indicates the +III oxidation state for iron. The temperature dependence is given by $\delta(T) = \delta_{T\to 0K} + \delta_{\rm SOD}$ and relates to the second-order Doppler shift ($\delta_{\rm SOD}$). From the latter, the Fe-site Mössbauer specific Debye-temperature $\Theta_M = 430(6)$ K in FeOCl is extracted, see Eq. (A1) given in the Appendix. Θ_M complies to the mean square vibrational velocity, $\langle v^2 \rangle$, of the iron nuclei. In addition, the Lamb-Mössbauer effect is related to the recoil-free fraction of a sample and thereby probes the mean-square (thermal) displacement, $\langle x^2 \rangle$, of the iron site. The temperature-dependence of the logarithm of the normalized integral intensities [Fig. 6(a)] is approximately linear and the corresponding $\Theta_{\rm LM} = 368(7)$ K can be obtained from a fit to the data using Eq. (A2), see Appendix. It appears that this value confirms the sample's crystalline quality in comparison with literature data [28]. These authors observed that rigorous exclusion of humidity leading to high quality samples, which are represented by $\Theta_{LM} = 327$ K. However, for standard treated samples (ambient atmosphere, exposure to moisture or solvents) Θ_{LM} is reduced, e.g., 267 K.

The spectra above 100 K (Fig. 5, top left) show a doublet arising from the electric quadrupole interaction at the iron nucleus. The quadrupole splitting (QS) is more than twice as large for FeOCl with cis-[FeO_4Cl_2] entities if compared to iron(III) oxides with [FeO_6] units (e.g., Fe_2O_3 [59]) and

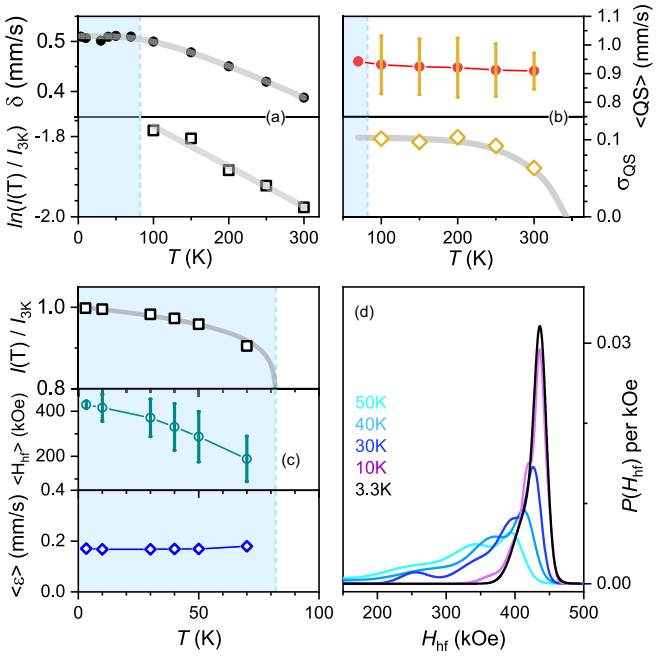

FIG. 6. Temperature dependence of the hyperfine parameters: symbols refer to experimental data and grey lines present fits to the data. (a) Center shift δ(T) and second-order Doppler effect. Lamb-Mössbauer effect derived from the normalized integral intensities. (b) Quadrupole splitting, QS, with bars illustrating the Gaussian distribution, σ_{QS}. (c) Power-law fit to the normalized integral intensities, average hyperfine magnetic field $H_{\rm hf}$(T) with Gaussian distribution (bars), and quadrupole shift ϵ. Dashed lines refer to the blocking temperature. (d) Distribution of $H_{\rm hf}$ for selected temperatures.

reflects the large anisotropy present in this quasi-2D compound. From computational work, we derived the electric field gradient (EFG) with the asymmetry parameter $\eta = 0.992$ (refined structure model, see Table I). The V_{zz} eigenvector is aligned with the b axis. From Eq. (A3) (see Appendix), we obtain $QS = -0.95$ mm/s in excellent agreement with our observation of 0.92(2) mm/s and previous paper [27–29]. Note that the experimental value derived from powder Mössbauer spectra gives always the absolute value of QS. Two aspects [Fig. 6(b)] are worth mentioning: (i) QS remains almost temperature independent and (ii) the spectral lines are broadened. The latter is taken into account by fitting the spectra using a Voigt-lineshape model (x-VBF Ref. [36]) with a Gaussian distribution $\sigma_{\rm QS}$. We attribute these features as an indication of a fast fluctuating regime existing below ≈360 K. For more details compare to the magnetic susceptibility for FeOCl given below.

In the temperature region below 100 K we observe a gradual development of magnetic spectra composed of sextets, see blue shaded areas in Fig. 5. The abrupt changes in integral intensities [Fig. 6(c)] indicate the onset of relaxation rates slower than the Larmor frequency f_L. We extrapolate a temperature of 82 K, which we relate to a blocking temperature T_b. Since we have no evidence for a λ anomaly from specific heat data around 80 K, see Figs. 3(b) and 3(c), we refrain from assigning this transition to LRO (T_N). A power-law fit to the integrated intensity yields the exponent $\beta = 0.1235(5)$ corresponding to the value of the Ising type (D = 2, d = 1) order parameter.

The Mössbauer spectrum at 70 K (Fig. 5, bottom left) is composed of a fast fluctuating fraction (doublet, ≈30%), which exhibits an asymmetrical lineshape. The magnetic contribution to the spectrum is fitted to a dynamic lineshape model [37]. Two slower relaxing fractions with flip frequencies close to $f_1 = 12.7$ and $f_2 = 15.8$ MHz ($\log f_{\rm av} = 7.2$) are obtained. These frequencies are comparable with the reported value of $\log f_{\rm av} \approx 6.7$ [30].

The low-temperature magnetically split spectra between 70 and 10 K (Fig. 5, blue-shaded areas) gradually develop into a sextet characterized by a distribution of hyperfine magnetic fields, $H_{\rm hf}$. This regime corresponds to persisting fluctuations (dynamics) and disparate orientations of the magnetic moment at individual Fe-sites relating to a spin-spiral scenario. The data analysis is shown in Figs. 6(c) and 6(d). As a result, the total Mössbauer spectra differ from the typical 3:2:1:1:2:3 intensity ratio of sextet lines expected for a single Fe site in the magnetically ordered state.

Below 10 K the relaxation times of the magnetically ordered sites are longer than the time window of the Mössbauer effect and thus the spectra appear static. For the fit of the Mössbauer spectrum at 3.3 K we employ a static Hamiltonian to derive individual hyperfine fields and their corresponding directions in space given by the polar and azimuth angles $\theta_{\rm Hq}$ and $\phi_{\rm Hq}$. Table IV provides the hyperfine parameters for the fit of the 3.3 K Mössbauer spectrum. The disparate site fractions, ϵ and $\phi_{\rm Hq}$ values of the individual components result in the overall broadening of the spectral lines. We found five magnetic components contributing to the observed Mössbauer spectrum (Table IV) with $H_{\rm hf}$ in the range 390–450 kOe. Note that the ordered moment is approximately one μ_B lower than the typical value for Fe^{III} (540 kOe) in hematite [59], with 100—110 kOe roughly corresponding to $1\mu_B$. Overall, the weighted averaged value of ≈4.2 μ_B is in agreement with the ordered moment of 4.1(4) μ_B from neutron data [33].

An incommensurate ground state with $H_{\rm hf}$ perpendicular to the principal axis of the EFG ($\theta_{\rm Hq} = 90°$) is established from an exact lineshape analysis of the Mössbauer spectrum at 3.3 K. It follows that the magnetic moments of the individual Fe sites are confined in the ac plane perpendicular to the chain direction. The orientation of the static magnetic moments of the five disparate Fe sites (1–5) are characterized by the azimuth angles ranging from 0° to 90°. Here $\phi_{\rm Hq} = 90°$ denotes $m \parallel [100]$ and $\phi_{\rm Hq} = 0°$ $m \parallel [001]$, respectively. The assignment is based on the anisotropy parameters (η), which is ≈0 (site 1) hence within the Fe–O layer. In contrast, the larger anisotropy with $\eta = 0.36$ accounts for any orientation involving the vdW stacking along the c axis. The reduced $\eta = 0.36$ relates to the magnetic phase of this quasi-2D material and is in agreement with the literature [25,27]. The site fraction of edge states amounts to ≈1.8% (site 6) and appears to be weakly correlated ($H_{\rm hf} \approx 70$ kOe). From an estimate of the ratio of surface to crystallite volume Fe-sites we would expect roughly 3% paramagnetic sites.

The evaluation of our experimental data provides insights into the presence of solitons. We start with the discussion of the enhanced linewidth ($\sigma_{\rm QS}$) between 82 K and 250 K (or up to $3 \times T_b$) indicating fast fluctuations, which are attributed

TABLE V. Soliton parameters for FeOCl. Values are given for the soliton energy (E_s), velocity (v_s), domain wall (d), and anisotropy parameter (D) at 82 K. The correlation length (ξ_s) and d are given in units of Fe-sites for 82 K and 20 K.

E_s (K)	v_s (m/s)	d	D (K)	ξ_s(82 K)	ξ_s(20 K)
82	640	13.7	0.24	12	129

to a flip rate Γ_a(T) in a dynamic scenario. In an antiferromagnetic chain the thermal activation energy of a soliton is given by $E_a \approx 2E_s$ and represents a soliton pair. We derive $E_a = 166(10)$ K from ln(Γ_a) versus the reciprocal temperature (Arrhenius plot). Thus, the soliton energy, $E_s \approx 82$ K and T_b are of the same order of magnitude. It follows that at temperatures above 250 K the solitons decay due to decreasing correlation length within the AFM chain, see Fig. 6(b). Below 82 K the persisting dynamics are altered with $f_s \leqslant f_L$ due to increasing interchain correlations within the Fe–O layer, see Fig. 6(c). In Table V we give the soliton parameters at 82 K calculated from Eqs. (A4)–(A6) given in the Appendix and Eq. (2).

E. Magnetic properties

Here we analyze and summarize the magnetic properties of FeOCl taking all above discussed features, specifically the evidence for nonlinear excitations (solitons) and finite-size effects into account. Corresponding magnetization data are shown in Figs. 7 and 8. We start with the temperature dependent susceptibility in small applied fields.

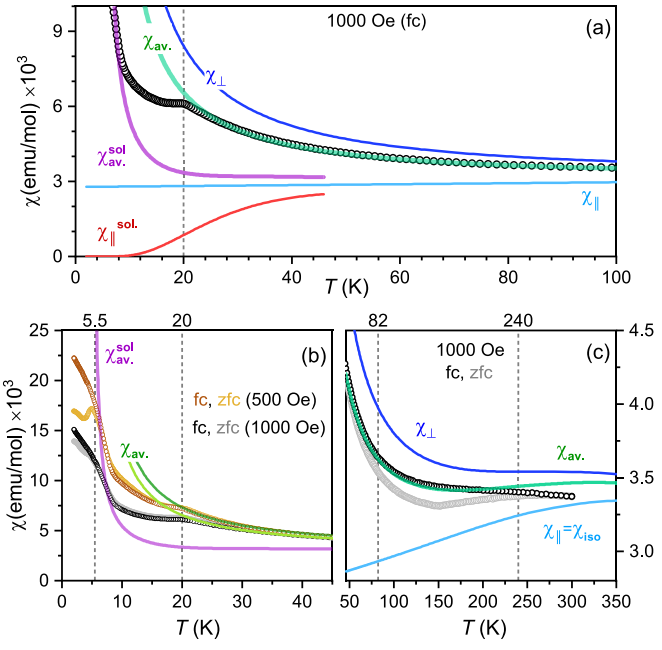

FIG. 7. (Top) Temperature dependence of the field-cooled (fc) and zero-field cooled (zfc) susceptibility for FeOCl. Results for the isotropic ($\chi_\parallel$), anisotropic ($\chi_{av.}$ with $\chi_\parallel \neq \chi_\perp$) AFM chain, and $\chi^{sol}_{av.}$ accounting for the soliton energy E_s with $\chi^{sol}_\parallel$ are presented for different temperature regimes.

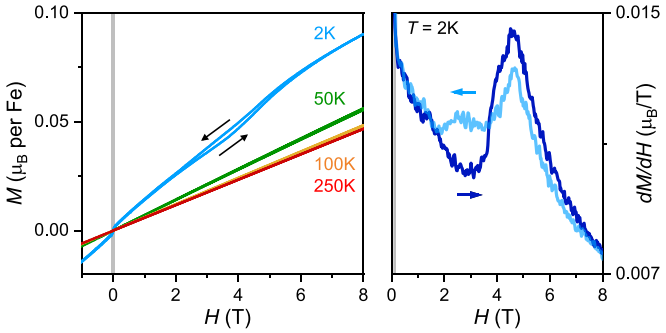

FIG. 8. (Left) Field dependence of the magnetization for FeOCl at selected temperatures. (Right) Field derivative of the magnetization at 2 K. The arrows indicate the direction of applied magnetic field change.

The fit of the magnetic susceptibility using the Bonner-Fisher model [60] for an isotropic Heisenberg $S = 5/2$ spin-chain system [Eqs. (A7) and (A8), Appendix] including a small amount of paramagnetic impurities of 1.5% (see also Table IV) gives a poor description of χ(T) at temperatures below 240 K. However, for high temperatures it allows for an estimate of $J \approx 45$ K (AFM), Fig. 7(c). T_{max} corresponds to the expected broad maximum around 360 K in agreement with literature data [31,32]. It can be seen in Fig. 7(c) that the measured susceptibility approaches $\chi_{iso} = \chi_\parallel$ only above 240 K concomitant with the decay of solitons above $3 \times T_b$ due to much shorter correlation lengths ξ of the antiferromagnetic chain.

In an axial anisotropic chain $\chi_\parallel \neq \chi_\perp$ is expected and deviation from the isotropic Heisenberg model manifests. More specific is the case of an underlying spin-spiral spin structure where two adjacent magnetic moments of the same sublattice along the dominating AFM chain are canted by an angle ϕ. This accounts for $\chi_\perp$(T) to increase faster than $\chi_\parallel$(T) with decreasing temperature, which results from an additional weak ferromagnetic contribution. According to Moriya [61] we derive $\chi_\perp$(T) using Eq. (1) (Ref. [62]),

$$\chi_\perp(T) = \chi_\parallel(T) \cdot (1 - \sin^2\phi) + \frac{C \cdot \sin^2\phi}{(T - \theta_{CW})}. \qquad (1)$$

Here, $\chi_\parallel$(T) refers to the isotropic AFM Heisenberg model with C the Curie constant, ϕ the canting angle, and Θ_{CW} the Curie-Weiss constant.

At temperatures above 20 K, we fitted the susceptibility data to $\chi_{av} = 1/3(\chi_\parallel + 2\chi_\perp)$ and obtain $\theta_{CW} \approx 5.0$ K, the canting angles $\phi = 8.0°$ ($H = 1000$ Oe) and $\phi = 8.8°$ ($H = 500$ Oe), respectively. We observe a difference between the zfc- and fc-cooling χ(T) data, see Fig. 7(c), between 82 K (in the vicinity of the blocking temperature, T_b) and 240 K. Referring to the Mössbauer results above, this regime relates to the thermal activation of solitons, which reveal their presence through a ferromagnetic component arising from DM interaction [61,63].

The experimental susceptibility data exhibits no anomaly around the blocking temperature of 82 K [Fig. 7(a)]. However, we observe a kink at 20 K, which is well in line with the small λ anomaly present in the zero field specific heat shown in Figs. 3(c) and 3(d). In Ising-like systems the inverse corre-

lation length diverges from the Heisenberg model and exhibits an exponential temperature dependence at low temperatures. Assuming that in the present case the spin-spiral chains are well described by nonlinear excitations (solitons) we express the temperature dependence of the inverse correlation length {Eq. (2), [20]} using the soliton energy $E_s \approx 82$ K, $J = 45$ K, and the anisotropy parameter $D \approx 0.24$ K,

$$\xi_{\mathrm{sol}}^{-1} = 2\sqrt{\frac{8DE_s}{\pi JT}}\exp(-E_s/T). \tag{2}$$

Inserting ξ_{sol}^{-1} into the Bonner-Fisher model, we find that $\chi_{\parallel}^{\mathrm{sol}}$ for $T \to 0$ K approaches smoothly zero. The difference in $\chi_{\parallel}$ develops rapidly below ≈45 K, see Fig. 7(a). The gradual change from χ_{av} to $\chi_{\mathrm{av}}^{\mathrm{sol}}$ below 20 K then accounts for the appearance of the kink. With respect to $\chi_{\perp}$ we note that the canting angle ϕ is concomitantly reduced to ≈4.6(1)° below 20 K marking the phase transition. Hence, the transition is marked by a change in the soliton dynamics by interchain correlations and presumably correlated to finite-size effects, see below. We recall, that the changes in dynamics are observed by Mössbauer spectroscopy and refer to Fig. 6(d) comparing the H_{hf} distribution at 30 K and 10 K.

Furthermore, FeOCl shows a transition at ≈5.5 K in accordance with the Curie-Weiss temperature, $\Theta_{\mathrm{CW}} \approx 5.0$ K derived above [Eq. (1)]. While the frustration within the Fe–O layers of the vdW compound with inherent competing AFM and FM exchange persists, the dipolar interaction between layers is antiferromagnetic, see also earlier neutron diffraction studies supporting the AFM ordering in the stacking direction [26,34]. Overall spin-glass behavior manifests below the freezing temperature $T_f \approx 5.5$ K as indicated by the divergence of zfc- and fc-susceptibility data in applied applied magnetic fields below ≈1200 Oe.

In Fig. 8 we show the field dependence of the magnetization. At high temperatures ($50\text{K} \leqslant T \leqslant 300\text{K}$) all data correspond to a low almost temperature independent linear paramagnetic response, reminiscent for strong AFM exchange. However, at 2 K (spin-glass-like phase) we observe spontaneous polarization in applied magnetic fields of ± 0.12 T. The spontaneous magnetization approximately relates to 1.3% Fe^{III} in reasonable agreement with the value obtained from Mössbauer spectroscopic experiments (Table IV) and may be attributed to edge states in this material. The slope of dM/dH (2 K) deviates from a straight line between 3.0 T and 5.8 T indicating a spin-flop transition at H_{sf} from spiral to fan like and the complete decay of soliton pairs. With decreasing field two consecutive transitions occur.

F. Conclusions

An unified understanding of the soliton-like evolution of magnetic fluctuations in FeOCl is achieved. From our experimental data we find $T_b = 82$ K, which we relate to a blocking temperature closely connected to the thermal activation energy of a single soliton E_s within an anisotropic, antiferromagnetic spin chain. T_b corresponds to literature values $T_N \approx 86\pm6$ K obtained from different experimental methods on large crystals, e.g., [31,32,34]. Conventional LRO in this temperature range can be ruled out based on the dynamics observed by Mössbauer spectroscopic experiments. In zero applied field, the λ anomaly corresponds to an entropy change of only 1% of a $S = 5/2$ spin system. This small entropy change is irrespective on the crystal size but occurs at ≈82 K for large crystals and around 20 K for microcrystalline powders. In both cases magnetoelastic coupling occurs, a structural phase transition from orthorhombic to monoclinic [32] and a change in the canting angle ϕ observed here. The latter corresponds to the canting ($2\phi \approx 9°$) of orthogonal chain segments below 20 K. This is in agreement with the incommensurate spin-spiral ground state with 99° derived from neutron diffraction at 4.2 K [33].

The order parameter obtained from Mössbauer spectroscopy below $T_b = 82$ K indicates 2D-Ising ordering. Hence, interchain interactions enforcing 2D ordering in the *ab* plane occur in a more gradual manner in finite-size particles, which is corroborated by persisting dynamics between 20 and 82 K. We calculated from ξ_{sol} at 20 K the number of correlated sites per chain along the *b* axis, which reaches the finite (crystallite) size (≈143 sites) of our particles. It follows that the remaining excitations are then those of a confined soliton pair (dimer) or a bound state. The latter has been referred to breathers in recent literature [22,23]. 2D fluctuations persist, given the finite size of only ≈ 440 sites in the *a* direction or ≈10 times the incommensurate modulation vector of 11/40 of the spin-spiral ground state. This implies persisting disorder (spin-glass-like phase with a freezing temperature around 5 K) as indicated by magnetic data in low applied magnetic fields.

In summary, we have introduced solitonic excitations of a nonlinear spin system with confinement to better understand the unconventional magnetic instability of the van der Waals material FeOCl. A detailed analysis of magnetization, specific heat, and Mössbauer spectroscopic data give evidence for a confinement of these solitons. Furthermore, their diffusional dynamics is supported by Raman scattering experiments. At this point we like to highlight that the observed phenomenology and proposed condensation of solitons into topological edge states is a generic feature of nonlinear systems with confinement [64]. It has recently been discussed for a broader range of systems, e.g., cavity polaritons in structured media and solitons in multimode fibers [65,66].

ACKNOWLEDGMENTS

Funding by the German Research Foundation (Deutsche Forschungsgemeinschaft, DFG) under the Projects No. 443703006 (CRC 1487) and No. 442589410 is gratefully acknowledged. P.L. and F.P. acknowledge support by the Deutsche Forschungsgemeinschaft, DFG/RTG Nanomet and EXC-2123 QuantumFrontiers 390837967. We thank W. Brenig and A. Saxena for discussions. Parts of this research were conducted using the supercomputer Mogon II and/or advisory services offered by Johannes Gutenberg University Mainz, which is a member of the AHRP (Alliance for High Performance Computing in Rhineland Palatinate) and the Gauss Alliance e.V.

APPENDIX

Here we give the equations used for the data analysis in Secs. III D and III E. References are provided in the main text.

Second-order Doppler effect. Relation to the Mössbauer specific Debye-temperature of Fe,

$$\delta_{\mathrm{SOD}}(T) = -A\left(\Theta_{\mathrm{M}} + 8T\left(\frac{T}{\Theta_{\mathrm{M}}}\right)^3 \int_0^{\Theta_{\mathrm{M}}/T} \frac{y^3}{e^y - 1}\, dy\right), \tag{A1}$$

$A = 9k_{\mathrm{B}}E_\gamma/16M_{\mathrm{eff}}c^2$, k_{B} (Boltzmann constant), $M_{\mathrm{eff}} = 53095\ \mathrm{MeV}/c^2$ (effective mass of the vibrating ^{57}Fe nuclei), and $E_\gamma = 14.413$ keV.

Lamb-Mössbauer effect. Relation of the recoil-free fraction to the mean-square (thermal) displacement of Fe,

$$\frac{d\ln(I(T)/I_{3K})}{dT} = \frac{-6E_R}{k_{\mathrm{B}}\Theta_{\mathrm{LM}}^2}. \tag{A2}$$

Here E_R refers to the recoil energy of the Mössbauer atom.

Quadrupole splitting. Relationship of QS and the electric field gradient,

$$QS = (eQV_{zz}/2)\sqrt{1 + \eta^2/3}. \tag{A3}$$

With e the positive charge of the proton and $Q = 0.16$ barn the quadrupole moment of ^{57}Fe, V_{zz} the principal component of the electric field gradient, and η the asymmetry parameter of the electric field gradient tensor.

Soliton parameter. E_s soliton energy, v_s soliton velocity, and d domain wall listed in Table V are obtained using the following equations given in Refs. [17,18,20,62],

$$E_s = 4S^2\sqrt{|D \cdot J|} \tag{A4}$$

$$v_s = \frac{4|J|S}{\sqrt{\frac{E_s}{2 \cdot T}}} \tag{A5}$$

$$d = \frac{4|J|S^2}{E_s} = \sqrt{\frac{|J|}{|D|}} \tag{A6}$$

Bonner-Fisher model. Description of the susceptibility of an isotropic chain,

$$\chi_{\mathrm{iso}}(T) = \frac{N_A g^2 \mu_B^2 S(S+1)}{3k_{\mathrm{B}}T} \cdot \frac{1+u}{1-u}. \tag{A7}$$

With N_A (Avogadro number), μ_B (Bohr magneton), g the Landé factor, J the AFM nearest-neighbor-coupling constant in units of Kelvin, and ξ the correlation length,

$$u = \coth\frac{2|J|S(S+1)}{T} - \frac{T}{2|J|S(S+1)} = -\exp(-\xi^{-1}). \tag{A8}$$

[1] T. P. Lyons, J. Puebla, K. Yamamoto, R. S. Deacon, Y. Hwang, K. Ishibashi, S. Maekawa, and Y. Otani, Acoustically driven magnon-phonon coupling in a layered antiferromagnet, Phys. Rev. Lett. **131**, 196701 (2023).

[2] Z. Qian, Z. Song, J. Wu, D. Wang, W. Wen, X. Wang, Y. Liu, and L. Xie, Chemical vapor deposition and Raman spectroscopy of two-dimensional antiferromagnetic FeOCl crystals, J. Phys. Chem. C **127**, 6785 (2023).

[3] M. Zhang, Q. Hu, Y. Huang, C. Hua, M. Cheng, Z. Liu, S. Song, F. Wang, H. Lu, P. He *et al.*, Spin-lattice coupled metamagnetism in frustrated van der Waals magnet CrOCl, Small **19**, 202300964 (2023).

[4] Y. Zeng, P. Gu, Z. Zhao, B. Zhang, Z. Lin, Y. Peng, W. Li, W. Zhao, Y. Leng, P. Tan *et al.*, 2D FeOCl: A highly in-plane anisotropic antiferromagnetic semiconductor synthesized via temperature-oscillation, chemical vapor transport, Adv. Mater. **34**, 2108847 (2022).

[5] D.-L. Bao, A. O'Hara, S. Du, and S. T. Pantelides, Tunable, ferroelectricity-inducing, spin-spiral magnetic ordering in monolayer FeOCl, Nano Lett. **22**, 3598 (2022).

[6] P. Gu, Y. Sun, C. Wang, Y. Peng, Y. Zhu, X. Cheng, K. Yuan, C. Lyu, X. Liu, Q. Tan *et al.*, Magnetic phase transitions and magnetoelastic coupling in a two-dimensional stripy antiferromagnet, Nano Lett. **22**, 1233 (2022).

[7] N. Miao, B. Xu, L. Zhu, J. Zhou, and Z. Sun, 2D intrinsic ferromagnets from van der Waals antiferromagnets, J. Am. Chem. Soc. **140**, 2417 (2018).

[8] M. Sun, C. Chu, F. Geng, X. Lu, J. Qu, J. Crittenden, M. Elimelech, and J.-H. Kim, Reinventing Fenton chemistry: Iron oxychloride nanosheet for pH-insensitive H_2O_2 activation, Environ. Sci. Technol. Lett. **5**, 186 (2018).

[9] T.-K. Ng, Edge states in antiferromagnetic quantum spin chains, Phys. Rev. B **50**, 555 (1994).

[10] S. Qin, T.-K. Ng, and Z.-B. Su, Edge states in open antiferromagnetic Heisenberg chains, Phys. Rev. B **52**, 12844 (1995).

[11] A. J. Friedman, B. Ware, R. Vasseur, and A. C. Potter, Topological edge modes without symmetry in quasiperiodically driven spin chains, Phys. Rev. B **105**, 115117 (2022).

[12] S. Mishra, G. Catarina, F. Wu, R. Ortiz, D. Jacob, K. Eimre, J. Ma, C. A. Pignedoli, X. Feng, P. Ruffieux, J. Fernández-Rossier, and R. Fasel, Observation of fractional edge excitations in nanographene spin chains, Nature (London) **598**, 287 (2021).

[13] L. Schneider, P. Beck, L. Rózsa, T. Posske, J. Wiebe, and R. Wiesendanger, Probing the topologically trivial nature of end states in antiferromagnetic atomic chains on superconductors, Nat. Commun. **14**, 2742 (2023).

[14] A. S. Davydov and N. I. Kislukha, Solitary excitons in one-dimensional molecular chains, Phys. Status Solidi (b) **59**, 465 (1973).

[15] L. F. Lemmens, I. Kimura, and W. J. M. de Jonge, Sine-Gordon kink solitons and the magnetisation in one-dimensional antiferromagnetic chains, J. Phys. C: Solid State Phys. **19**, 139 (1986).

[16] S. Rakhmanova and D. L. Mills, Nonlinear spin excitations in finite Heisenberg chains, Phys. Rev. B **54**, 9225 (1996).

[17] L. J. de Jongh, Solitons in magnetic chains, J. Appl. Phys. **53**, 8018 (1982).

[18] H. J. M. de Groot, L. J. de Jongh, M. Elmassalami, H. H. A. Smit, and R. C. Thiel, Mössbauer relaxation studies of

non-linear dynamical excitations in low-dimensional magnets, Hyperfine Interact. **27**, 93 (1986).
[19] H. Smit, H. de Groot, M. Elmassalami, R. Thiel, and L. de Jongh, Non-linear excitations in Ising-type magnetic chain systems I, Phys. B: Condens. Matter **154**, 237 (1989).
[20] A. Krimmel, R. Stief, J. Pebler, L.-P. Regnault, and M. Ohl, Spin dynamics of the one-dimensional magnet Na_2MnF_5, Phys. Rev. B **67**, 024405 (2003).
[21] J.-I. Kishine, I. G. Bostrem, A. S. Ovchinnikov, and V. E. Sinitsyn, Topological magnetization jumps in a confined chiral soliton lattice, Phys. Rev. B **89**, 014419 (2014).
[22] T. E. Rebecca, A. L. Felcy, and M. M. Latha, Localized spin excitations in a site-dependent antiferromagnetic spin system with D-M interaction, Eur. Phys. J. B **92**, 188 (2019).
[23] I. G. Bostrem, V. E. Sinitsyn, A. S. Ovchinnikov, E. G. Ekomasov, and J. Kishine, Discrete magnetic breathers in monoaxial chiral helimagnet, AIP Adv. **11**, 10.1063/9.0000045, 015208 (2021).
[24] H. Schäfer, F. E. Wittig, and M. Jori, Untersuchungen am System Fe_2O_3–$FeCl_3$–H_2O–HCl. IX Die thermochemische Beständigkeit des Eisenoxychlorids FeOCl, Z. Anorg. Allg. Chem. **287**, 61 (1956).
[25] E. Kostiner and J. Steger, Mössbauer effect study of FeOCl, J. Solid State Chem. **3**, 273 (1971).
[26] R. W. Grant, Magnetic structure of FeOCl, J. Appl. Phys. **42**, 1619 (1971).
[27] R. W. Grant, H. Wiedersich, R. M. Housley, G. P. Espinosa, and J. O. Artman, Mössbauer determination of Fe^{57} nuclear quadrupole coupling parameters in ferric oxychloride, Phys. Rev. B **3**, 678 (1971).
[28] R. H. Herber and Y. Maeda, Lattice dynamics and hyperfine interactions of layer compounds from ^{57}Fe Mössbauer spectroscopy: FeOCl, Phys. B: Condens. Matter **99**, 352 (1980).
[29] R. H. Herber and A. Salmon, Hyperfine interactions in the anisotropic layer compound FeOCl from ^{57}Fe Mössbauer studies, Hyperfine Interact. **33**, 133 (1987).
[30] Y.-D. Dai, Z. Yu, Y. He, H.-B. Huang, T. Shao, J. Lin, A. M. Ali, Z.-Y. Jiang, and Y.-F. Hsia, Mössbauer studies on the spiral antiferromagnetic coupling in iron oxychloride, Chem. Phys. Lett. **358**, 473 (2002).
[31] R. Bannwart, J. Phillips, and R. Herber, Magnetic susceptibility of FeOCl, J. Solid State Chem. **71**, 540 (1987).
[32] J. Zhang, A. Wölfel, L. Li, S. van Smaalen, H. L. Williamson, and R. K. Kremer, Magnetoelastic coupling in the incommensurate antiferromagnetic phase of FeOCl, Phys. Rev. B **86**, 134428 (2012).
[33] A. Adam and G. Buisson, Structure magnétique cyclo'dale de FeOCl, Phys. Status Solidi (a) **30**, 323 (1975).
[34] S. R. Hwang, W.-H. Li, K. C. Lee, J. W. Lynn, and C.-G. Wu, Spiral magnetic structure of Fe in van der Waals gapped FeOCl and polyaniline-intercalated FeOCl, Phys. Rev. B **62**, 14157 (2000).
[35] K. Lagarec and D. Rancourt, *Recoil - Mössbauer spectral analysis software for Windows*, Department of Physics, University of Ottawa, ON, Canada, version 1.0 ed. (1998).
[36] K. Lagarec and D. Rancourt, Extended Voigt-based analytic lineshape method for determining *N*-dimensional correlated hyperfine parameter distributions in Mössbauer spectroscopy, Nucl. Instrum. Methods Phys. Res., Sect. B **129**, 266 (1997).
[37] M. Blume and J. A. Tjon, Mössbauer spectra in a fluctuating environment, Phys. Rev. **165**, 446 (1968).
[38] M. Profeta, C. Pickard, and F. Mauri, Accurate first principles prediction of ^{17}O NMR parameters in SiO_2: Assignment of the zeolite ferrierite spectrum, J. Am. Chem. Soc. **125**, 541 (2003).
[39] S. J. Clark, M. D. Segall, C. J. Pickard, P. J. Hasnip, M. J. Probert, K. Refson, and M. Payne, First principles methods using CASTEP, Z. Kristall. **220**, 567 (2005).
[40] H. J. Monkhorst and J. D. Pack, Special points for Brillouin-zone integrations, Phys. Rev. B **13**, 5188 (1976).
[41] A. A. Coelho, *TOPAS* and *TOPAS*-Academic: An optimization program integrating computer algebra and crystallographic objects written in C++, J. Appl. Cryst. **51**, 210 (2018).
[42] M. D. Lind, Refinement of the crystal structure of iron oxychloride, Acta Cryst. B **26**, 1058 (1970).
[43] P. Javadian, T. K. Nielsen, D. B. Ravnsbæk, L. H. Jepsen, M. Polanski, T. Plocinski, I. Kunce, F. Besenbacher, J. Bystrzycki, and T. R. Jensen, Scandium functionalized carbon aerogel: Synthesis of nanoparticles and structure of a new ScOCl and properties of $NaAlH_4$ as a function of pore size, J. Solid State Chem. **231**, 190 (2015).
[44] L. Jongen and G. Meyer, Scandium(III) oxide bromide, ScOBr, Acta Cryst. E **61**, i153 (2005).
[45] E. Gamsjäger and M. Wiessner, Low temperature heat capacities and thermodynamic functions described by Debye–Einstein integrals, Monatsh. Chem. **149**, 357 (2018).
[46] L. Pisani, R. Valentí, B. Montanari, and N. M. Harrison, Density functional study of the electronic and vibrational properties of TiOCl, Phys. Rev. B **76**, 235126 (2007).
[47] D. Fausti, T. T. A. Lummen, C. Angelescu, R. Macovez, J. Luzon, R. Broer, P. Rudolf, P. H. M. van Loosdrecht, N. Tristan, B. Büchner, S. van Smaalen, A. Möller, G. Meyer, and T. Taetz, Symmetry disquisition on the TiOX phase diagram (X = Br, Cl), Phys. Rev. B **75**, 245114 (2007).
[48] P. Lemmens, K. Y. Choi, G. Caimi, L. Degiorgi, N. N. Kovaleva, A. Seidel, and F. C. Chou, Giant phonon softening in the pseudogap phase of the quantum spin system TiOCl, Phys. Rev. B **70**, 134429 (2004).
[49] P. Lemmens, K. Y. Choi, R. Valentí, T. Saha-Dasgupta, E. Abel, Y. S. Lee, and F. C. Chou, Spin gap formation in the quantum spin systems TiOX, X = Cl and Br, New. J. Phys. **7**, 74 (2005).
[50] M. Balkanski, R. F. Wallis, and E. Haro, Anharmonic effects in light scattering due to optical phonons in silicon, Phys. Rev. B **28**, 1928 (1983).
[51] P. Yogi, S. K. Saxena, S. Mishra, H. M. Rai, R. Late, V. Kumar, B. Joshi, P. R. Sagdeo, and R. Kumar, Interplay between phonon confinement and Fano effect on Raman line shape for semiconductor nanostructures, analytical study, Solid State Commun. **230**, 25 (2016).
[52] V. I. Korepanov and H. Hamaguchi, Quantum-chemical perspective of nanoscale Raman spectroscopy with the three-dimensional phonon confinement model, J. Raman Spectr. **48**, 842 (2017).
[53] P. Richards and W. Brya, Spin-fluctuation light scattering at high temperature, Phys. Rev. B **9**, 3044 (1974).
[54] H. Haken, *Synergetics. An Introduction* (Springer-Verlag, Berlin, 1977).

[55] P. Lemmens, G. Güntherodt, and C. Gros, Magnetic light scattering in low-dimensional quantum spin systems, Phys. Rep. **375**, 1 (2003).

[56] V. I. Korepanov and D. M. Sedlovets, An asymmetric fitting function for condensed-phase Raman spectroscopy, Analyst **143**, 2674 (2018).

[57] P. Gütlich, E. Bill, and A. X. Trautwein, *Mössbauer Spectroscopy and Transition Metal Chemistry, Fundamentals and Applications* (Springer, Berlin, 2011).

[58] F. Grandjean and G. J. Long, Best practices and protocols in Mössbauer spectroscopy, Chem. Mater. **33**, 3878 (2021).

[59] E. D. Grave and R. E. Vandenberghe, Mössbauer effect study of the spin structure in natural hematites, Phys. Chem. Miner. **17**, 344 (1990).

[60] M. E. Fisher, Magnetism in one-dimensional systems—The Heisenberg model for infinite spin, Am. J. Phys. **32**, 343 (1964).

[61] T. Moriya, Anisotropic superexchange interaction and weak ferromagnetism, Phys. Rev. **120**, 91 (1960).

[62] J. Pebler, C. Frommen, M. Mangold, R. Stief, A. Krimmel, R. van de Kamp, M. Ohl, and L.-P. Regnault, Comparison of the non-linear spin dynamics in antiferromagnetic chain compounds Na_2MnF_5 and $(ND_4)_2MnF_5$, Z. Anorg. Allg. Chem. **630**, 829 (2004).

[63] I. Dzyaloshinsky, A thermodynamic theory of weak ferromagnetism of antiferromagnetics, J. Phys. Chem. Solids **4**, 241 (1958).

[64] A. Saxena, P. G. Kevrekidis, and J. Cuevas-Maraver, Nonlinearity and topology, in *Emerging Frontiers in Nonlinear Science*, edited by P. G. Kevrekidis, J. Cuevas-Maraver, and A. Saxena (Springer International Publishing, Cham, 2020), pp. 25–54.

[65] D. Tanese, H. Flayac, D. Solnyshkov, A. Amo, A. Lemaître, E. Galopin, R. Braive, P. Senellart, I. Sagnes, G. Malpuech, and J. Bloch, Polariton condensation in solitonic gap states in a one-dimensional periodic potential, Nat. Commun. **4**, 1749 (2013).

[66] M. Zitelli, F. Mangini, and S. Wabnitz, Statistics of modal condensation in nonlinear multimode fibers, Nat. Commun. **15**, 1149 (2024).